Received: 4 November 2020 | Accepted: 13 November 2020

DOI: 10.1111/ter.12512

RESEARCH ARTICLE

Terra Nova WILEY

First record of OSL-dated fluvial sands in a tropical Andean cave reveals rapid late Quaternary tectonic uplift

Patrice Baby[1,2] | Willem Viveen[2] | Jorge Sanjurjo-Sanchez[2,3] | Jean-Yves Bigot[4] | Antony Dosseto[5] | Juan C. Villegas-Lanza[6] | James Apaéstegui[6] | Jean-Loup Guyot[1]

[1]GET-UMR CNRS/IRD/Univ. Paul Sabatier, Toulouse, France

[2]Grupo de Investigación en Geología Sedimentaria, Departamento de Ingeniería, Pontificia Univ. Católica del Perú, Lima, Perú

[3]Instituto Universitario de Geología "Isidro Parga Pondal", Univ. de A Coruña, A Coruña, Spain

[4]Association Française de Karstologie (AFK), Montpellier, France

[5]Wollongong Isotope Geochronology Laboratory, School of Earth, Atmospheric and Life Sciences, Univ. of Wollongong, Wollongong, NSW, Australia

[6]Instituto Geofísico del Perú, Lima, Peru

Correspondence
Patrice Baby, GET-UMR CNRS/IRD/Univ. Paul Sabatier, 14 Avenue Edouard Belin, 31400 Toulouse, France.
Email: patrice.baby@ird.fr

Funding information
IPGH PAT-GEOF07; Pontificia Universidad Católica del Perú; Xunta de Galicia, Spain

Abstract

We present the first results of OSL-dated fluvial sands extracted from a riverside cave in the tropical Andes. The excellent agreement between the ages of the various samples allowed the calculation of a late Quaternary valley incision rate forced by ongoing uplift of an active Subandean fault-propagation fold in NE Peru. A structural cross-section was constructed to understand the relationship between the geometry of the fault-propagation fold, historical damaging earthquakes and the cave system. The calculated uplift rate is 2.3 to 2.6 mm a^{-1} over the past 70 ka and can be directly linked to active propagation of west-verging basement thrusts. It is similar to uplift rates calculated from fluvial terraces in the Subandes of Colombia and Venezuela. The results will help to better assess the seismic hazard and confirm that OSL dating of fluvial sands in caves is a powerful tool to quantify uplift rates of active mountain fronts.

1 | INTRODUCTION

The evaluation of fluvial incision in mountain ranges is used to quantify tectonic uplift rates if other possible factors causing local base level fall are not applicable (Burbank & Anderson, 2011). Such factors may include changes in fluvial discharge caused by long-term climate forcing (Bridgland & Westaway, 2008), river capture (Antón et al., 2012), glacio-eustatic changes (Viveen et al., 2013) or lake drainage (Viveen et al., 2019).

The South American Subandean fold and thrust belt is tectonically highly active, and crustal movements and associated seismicity pose a significant geohazard to the local population, particularly in NE Peru (Devlin et al., 2012; Tavera et al., 2001; Villegas-Lanza et al., 2016). Tectonic deformation in this area is related to west-verging, basement-involved, fault-propagation folds (Calderon et al., 2017). Long-term tectonic uplift rates of the eastern Peruvian orogenic wedge have been calculated from low-temperature thermochronology (Eude et al., 2015 and references therein), but only one study is available so far for the late Quaternary (Viveen et al., 2020). This is probably due to the difficult terrain conditions in Andean tropical valleys that limit access to outcrops and geological-geomorphological field mapping. High precipitation, and consequently, high erosion rates (Armijos et al., 2013) further hamper the long-term preservation of landforms that can be used to quantify tectonic uplift rates. The northern Peruvian Subandean zone is an important tropical karst region due to the presence of thick Triassic-Jurassic carbonate series (Rosas et al., 2007). In such a geological context, one way to compensate for the lack of landforms is to find horizontal fossil caves in the flanks of the river valleys, where exogenous sediments can be preserved and used as substitutes to calculate incision rates (Calvet et al., 2015; Haeuselmann et al., 2007; Harmand et al., 2017; Stock et al., 2005; Stock et al., 2005; Wagner et al., 2011).

Here we present, the first results of optically stimulated luminescence (OSL)-dated fluvial sands extracted from a riverside cave in the tropical Subandes. The study focuses on the NW-SE oriented Cerro Blanco anticline (Calderon, Baby, Hurtado, et al., 2017), which constitutes, with a lateral extension of over 60 km, the western flank of the Moyobamba Basin at the boundary between the Eastern Cordillera and the Subandes (Figure 1). The excellent agreement between the ages of the various samples allows the calculation of late Quaternary valley incision rates forced by ongoing uplift of this active fault-propagation fold. The calculated tectonic uplift rate is only the second published, late Quaternary uplift rate available for the Peruvian Subandean region (Viveen et al., 2020) and one of the very few for the entire Subandes (Bes de Berc et al., 2005; Guzman et al., 2013; Veloza et al., 2015). It testifies intense neotectonic activity and will allow a better assessment of the seismic hazard of the Moyobamba region.

Statement of significance

Dating of fluvial sands in cave is a powerful tool to quantify Quaternary incision and uplift rates of active mountain fronts. For the first time in the Andes, we present results of OSL-dated fluvial sands extracted from a riverside cave. The excellent agreement between the ages of the various samples allowed the calculation of late Quaternary valley incision rate forced by ongoing uplift of an active Subandean fault-propagation fold of the tropical north-eastern Peru. We also show that this fold is related to a west-verging basement fault at the origin of historical damaging earthquakes. The calculated uplift rate is relatively high, but consistent with the sparse results obtained in other Subandean regions. This study has been achieved through well-constrained multidisciplinary researches, bringing experts from 4 countries. It will certainly help in a better assessment of the seismic hazard of the study area. This model could serve as a basis for future works in tropical karstic mountain fronts.

2 | THE CERRO BLANCO BASEMENT–INVOLVED FAULT–PROPAGATION FOLD

The Cerro Blanco and Moyobamba Basin structural architecture was analysed at regional scale and integrated in a balanced cross-section constructed from the Eastern Cordillera to the Amazonian lowland (Calderon, Baby, Hurtado, et al., 2017). These authors showed that the west-verging basement thrust associated with the fold could be the origin of the magnitude 6.6–6.4 Mw Moyobamba 1990 and 1991 damaging earthquakes (Tavera et al., 2001) (Figure 1). The focal mechanism solutions of these earthquakes are consistent with thrust fault ruptures located between 25 and 30 km depth (Devlin et al., 2012) (Figure 2). The fault emerges at the surface NW of the anticline (Figures 1 and 2). The Cerro Blanco fault-propagation fold deformed a sedimentary series constituted by Triassic clastic rift deposits, thick late Triassic-early Jurassic post-rift carbonates (Rosas et al., 2007), late Jurassic red beds, Cretaceous fluvial to shallow marine deposits, and late Cenozoic deposits of the Moyobamba Basin (Rodríguez et al., 2017). The Neogene sequence recorded the development of the modern syn-orogenic Moyobamba Basin in a lacustrine environment evolving progressively to an alluvial system. Seismic reflection data show a maximum thickness of 3,000 m of Neogene sediments (Calderon, Baby, Hurtado, et al., 2017). The Cerro Blanco fold core is formed by Palaeozoic metasediments. Fold propagation started during the Neogene inversion of the Triassic-Jurassic extensional basin (Calderon, Baby, Hurtado, et al., 2017). At the western border of the Moyobamba Basin, late Neogene deposits are weakly tilted on the eastern limb of the Cerro Blanco anticline (Figure 1). The late Triassic-early Jurassic carbonates of the eastern limb have been exposed to long-term incision and speleogenesis. Recent explorations of the karst showed the presence of important cave systems in the Cerro Blanco (Bigot et al., 2018; Klein et al., 2015). One of them is the Tishuca Cave, which is a horizontal fossil riverside cave located in the northern part of the anticline, at a relative elevation of 159 m above the adjacent Mayo river (Figure 2).

3 | THE TISHUCA CAVE AND ITS SEDIMENTARY ARCHIVE

The structural cross-section (Figure 2) illustrates the tectonic and geomorphologic framework of the Tishuca cave speleogenesis. The cave entrance is located in the tropical forest (–77.5782°, –5.7301°) at an altitude of 1,120 m asl. (Figure 3.1). It developed in the limestones of the Triassic Chambara Fm., with a total thickness of around 2000 m. In the cave, limestone bed thicknesses vary between 0.5 and 2 m and structural dip plunges 25° to the NE (Figure 3). The cave is 700 m long and consists of a single, 20-m-wide fossil gallery, which developed by following the N130° direction of the structural dip, parallel to the adjacent Mayo River valley (Figure 3.1). This single duct presents a chaotic floor dotted with collapsed blocks and some shafts. The parietal forms, which make it possible to define the type of excavation, are not preserved, probably due to significant vault tearing (falling blocks). The only interpretable elements are the longitudinal profile of the cavity and the dip of the limestone strata. This dip was exploited by running water, which gave its subhorizontal profile to the cave, suggesting that a local base level controlled its formation. Similar fossil caves – with a general slope of 1.5% - have been explored below the Tishuca Cave at different altitude levels (Klein et al., 2015, 2016; Robert et al., 2020). All these caves seem to indicate that subterranean rivers regularised their profiles in relation to a base level undergoing constant uplift. The upper part of the Cerro Blanco anticline has not yet been explored, but certainly contains the same type of cavities.

In the part least affected by the collapsing blocks of the Tishuca Cave, flowstones seal exogenous fluvial sediments (Figure 3.3)

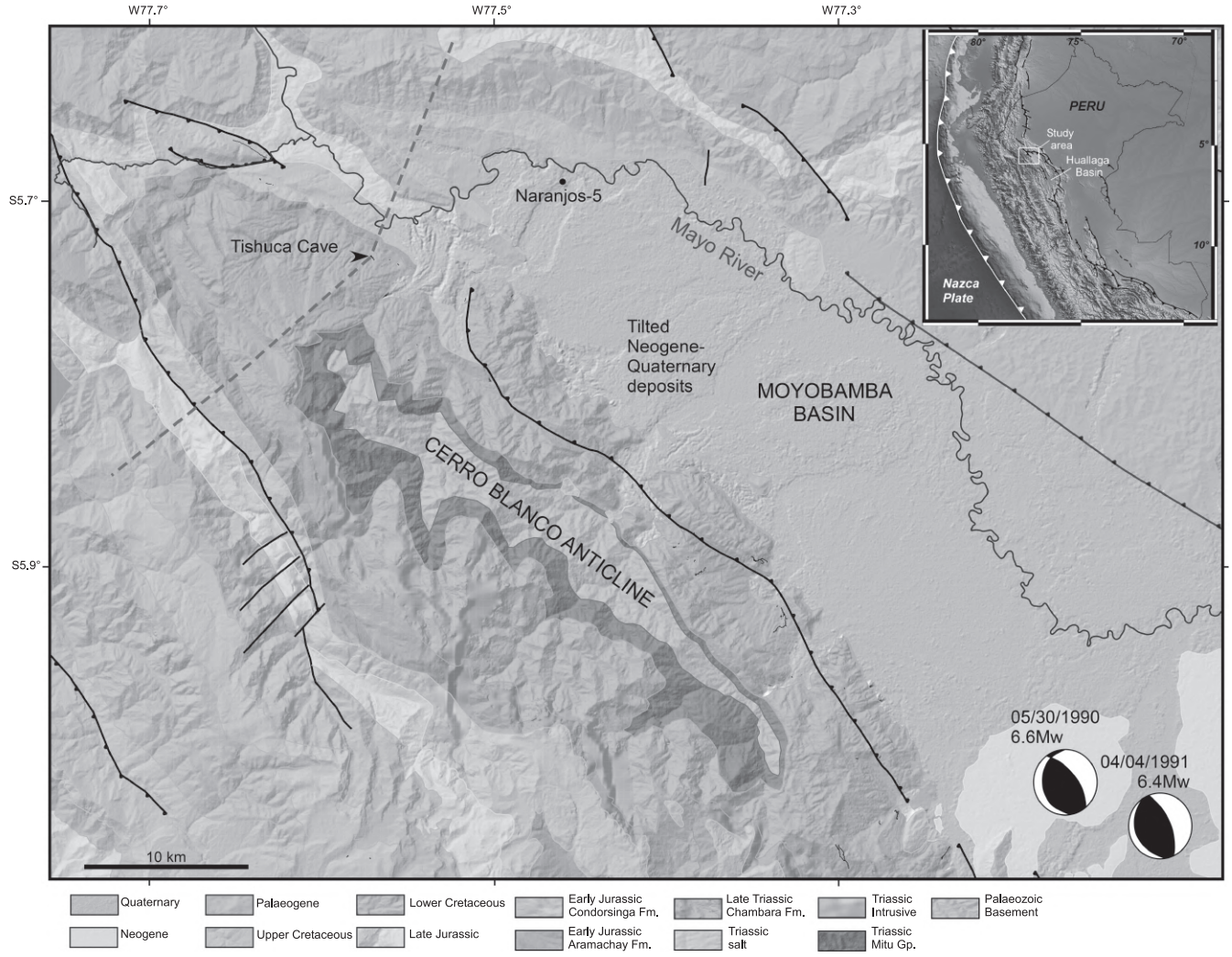

FIGURE 1 Geologic map of the study area (modified from the INGEMMET geological maps of Peru), with the location of the Tishuca Cave and the sampling site Naranjos-5, in late Quaternary sediments of the Mayo River. The red dashed line shows the location of the cross-section in Figure 2. Focal mechanisms solutions are displayed from the two largest reverse-fault crustal damaging earthquakes that occurred recently in this area (Devlin et al., 2012). Labels indicate date and moment magnitude (Figure 2). [Colour figure can be viewed at wileyonlinelibrary.com]

that occupies a lower level accessible through a semi-vertical shaft (Figure 3.2 and 3.4). The gallery cross-section (Figure 3.2) illustrates the architecture of the cave along this access point. It shows how the cave recorded a base level lowering that moved towards the NE, as the Mayo River is doing now (Figure 2).

The discovered exogenous sediments, which are located 26 m below the cave entrance (Figure 3.1 and 3.2), are well-preserved in a two-metre-thick stratigraphic sequence (Figure 3.3) that contains medium to very coarse, poorly sorted, sub-rounded sands with planar cross-beds (lithofacies *Sp* according to the classification of Miall, 1996). The quartz content of the fine sand fraction ranges from 72.9% to 83.0% and the content of feldspars from 13.8% to 21.8%. Heavy minerals vary from 3.2% to 5.3%, and contain biotite, siderite and goethite as detected by X-Ray Diffraction Analysis (XRD) in bulk samples (Figure 4).

Mineralogical and geochemical analysis of Tishuca sands are comparable to those obtained from terrace sediments of the Mayo River basin (Naranjos-5, Figure 4). This terrace is located approximately 50 m above the river floodplain level and has a late Quaternary age. This sample location was chosen because a late Quaternary sediment sample has been exposed longer to weathering processes when compared e.g. to a sample from the current river bed. Post-depositional weathering processes and their effects on sample geochemistry and mineralogy should therefore be more

FIGURE 2 Structural cross-section through the Cerro Blanco basement-involved fault-propagation fold showing the tectonic framework and the geometric relationships between the Tishuca Cave and the Mayo River valley. The two focal mechanism earthquakes shown in Figure 1 are projected onto the vertical profile (focal mechanisms and depths taken from Devlin et al., 2012). [Colour figure can be viewed at wileyonlinelibrary.com]

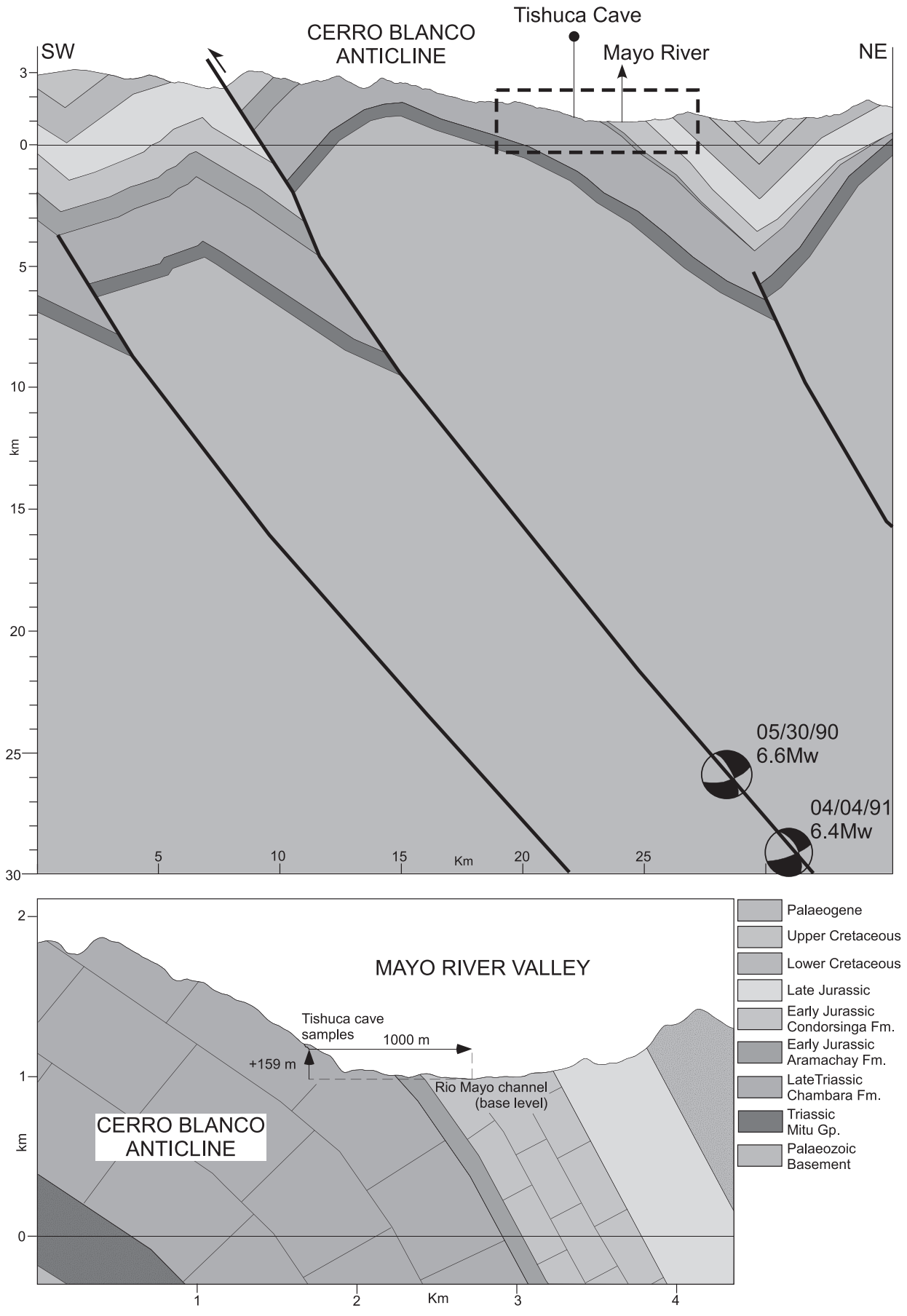
Tishuca Cave
CERRO BLANCO
ANTICLINE
Mayo River
SW
NE
3
0
5
10
15
20
25
30
km
05/30/90
6.6Mw
04/04/91
6.4Mw
5
10
15
Km
20
25
2
1
0
km
MAYO RIVER VALLEY
Tishuca cave
samples
1000 m
+159 m
Rio Mayo channel
(base level)
CERRO BLANCO
ANTICLINE
1
2
Km
3
4
Palaeogene
Upper Cretaceous
Lower Cretaceous
Late Jurassic
Early Jurassic
Condorsinga Fm.
Early Jurassic
Aramachay Fm.
LateTriassic
Chambara Fm.
Triassic
Mitu Gp.
Palaeozoic
Basement

similar between the late Quaternary Tishuca cave sands and the late Quaternary Mayo River basin sample, resulting in a lower bias when comparing the samples. Palaeo-current reconstructions on the basis of the foresets of the Tishuca sands show a south-easterly direction of the palaeo-flow, similar to the flow direction of the present-day Mayo River.

Thus, the orientation and the morphology of the cave, the mineralogical similarity of the cave sands to the Mayo River basin sediments, and the foreset orientation suggest a period of NW-SE enhanced fluvial activity that took place in a former passage of the Mayo River. The sands were carefully sampled for OSL dating. The Mayo River meanders across the current Moyobamba Basin floodplain (Figure 1) located 159 m below the position of the analysed cave sands (Figure 2). It is disconnected from a marine base level and can therefore be considered as the present-day local base level. Thus, we assume that the Tishuca horizontal fossil cave recorded an ancient level of the Mayo River, and can be used as a geomorphic marker to calculate a regional incision rate of the Mayo Valley since the deposition of the Tishuca sands. Similar examples of local base level records exist in other karstic mountain environments (Calvet et al., 2015; Harmand et al., 2017; Liu et al., 2014).

4 | SEDIMENT DEPOSITIONAL CHRONOLOGY

Three samples were taken for OSL dating by hammering steel cores in bedding-parallel direction into the sand deposit from the top to the bottom at 0.2 m (Tishuca-1), 0.8 m (Tishuca-3) and 1.6 m (Tishuca-2) depth. The tubes were opened under subdued red light in the Luminescence Laboratory of the University of A Coruña. Quartz grains of the fine sand fraction (180–250 μm) from the central part of the cores were separated by procedures described in Viveen et al. (2014).

The blue OSL signal of multigrain quartz aliquots was measured in an automated Risø DA-15 TI/OSL reader system equipped with blue (470 ± 30 nm) light-emitting diodes (LEDs) for stimulation. Signals were measured using a 9235QA photomultiplier tube (PMT) with an optical Hoya U-340 filter of 6 mm thick (340 ± 80 nm emission), placed between the aliquots and the PMT. Beta doses were given to aliquots using a $^{90}Sr/^{90}Y$ beta source emitting a 0.090 ± 0.003 Gy/s dose.

The blue-OSL (BL-OSL) single-aliquot regenerative dose (SAR) protocol (Murray & Wintle, 2000) was used to estimate the equivalent doses (D_es). After performing preheat tests, a preheat temperature of 240°C for 10 s was established before the OSL measurements. Dose recovery tests were performed (Murray & Wintle, 2003) on aliquots previously bleached with blue light and irradiated with beta doses similar to the calculated D_es.

The dose-rate (D_r) was estimated using Low Background Gamma Spectrometry on bulk samples, measuring the ^{238}U, ^{235}U, ^{232}Th and ^{40}K decay chain activities in a coaxial Canberra XTRA gamma detector (Ge Intrinsic; model GR6022) located within a 10-cm-thick lead shield. For conversion, the factors of Guérin et al. (2011) were used. The alpha contribution was neglected and the beta dose-rate was corrected assuming that the HF etching step of quartz grains had removed the surface layer of the grain (Brennan, 2003). Both the water content and saturation of the samples were assessed in the laboratory by weighing before and after drying, and by measuring the maximum water content of saturated samples. Cosmic dose rates were calculated according to Prescott and Hutton (1994).

The gamma spectrometry provided similar results for ^{238}U and ^{232}Th decay-chains and for ^{40}K activities of all samples (Table 1). ^{235}U activity concentration was below detection limits, while both ^{232}Th and ^{238}U decay-chains did not show disequilibrium. An average water content of 20 ± 3% was used, as saturation was above 25% in all samples, and air humidity inside caves is usually near saturation values. Resulting D_rs ranged from 0.96 ± 0.10 Gy ka^{-1} to 1.08 ± 0.04 Gy ka^{-1} (Table 1). These D_rs were very similar, and fit the similar mineralogical and chemical composition observed for all three sand samples (Figure 4). We can therefore safely assume a single depositional event for the sands.

Quartz multigrain aliquots exhibited weak and dim OSL signals, but fast decay. Typical OSL signal and growth curves for the samples are provided in Figure 5. The natural and regenerated signals decayed more than ca. 80% in the first two seconds of stimulation and more than ca. 90% for the first five seconds. This corresponds to a fast decay although signals were weak. Natural signals usually range between 400 and 2000 cts in the first 0.2 s of stimulation, while beta irradiation with 50 Gy to regenerate OSL signals usually shows a similar response. The weak OSL signals limited the use of small aliquots, so a first test was performed to choose the proper aliquot size. For the three samples, a set of 24 multigrain aliquots composed of 20–30 grains (1 mm diameter size) was measured and compared to a set of 24 aliquots composed of 80–100 grains (2 mm diameter size). Both the obtained signals and equivalent doses (D_e) were similar, but the 1 mm diameter size aliquots provided a higher number of rejected aliquots due to the lack of significant OSL signals. Thus, the larger aliquot size was selected for the assessment of the D_es. Despite this, around 75% of the aliquots in the three samples was rejected due to either too weak signals (no signal response to dose), or because they did not meet the SAR requirements (Table 1), which is a recycling ratio within the range 0.9–1.1 and a recuperation below 0.1 (Murray & Wintle, 2003). Testing therefore continued until more than 40 accepted aliquots were obtained.

The obtained D_es distributions of the accepted aliquots provided dispersed symmetric and weakly skewed distributions with kurtosis values ranging from 2 to 2.5. The high dispersion can be observed in Kernel Density Estimation plots and Radial Plots (Figure 6). Overdispersion values of the central age (Galbraith et al., 1999) were slightly above 30% for samples Tishuca-2 and Tishuca-3, and higher for Tishuca-1, as intrinsic overdispersion was deduced from dose recovery tests between 12%–20% (Table 1). The low overdispersion obtained after subtracting the intrinsic overdispersion and the symmetric distributions indicated that there was no evidence of partial

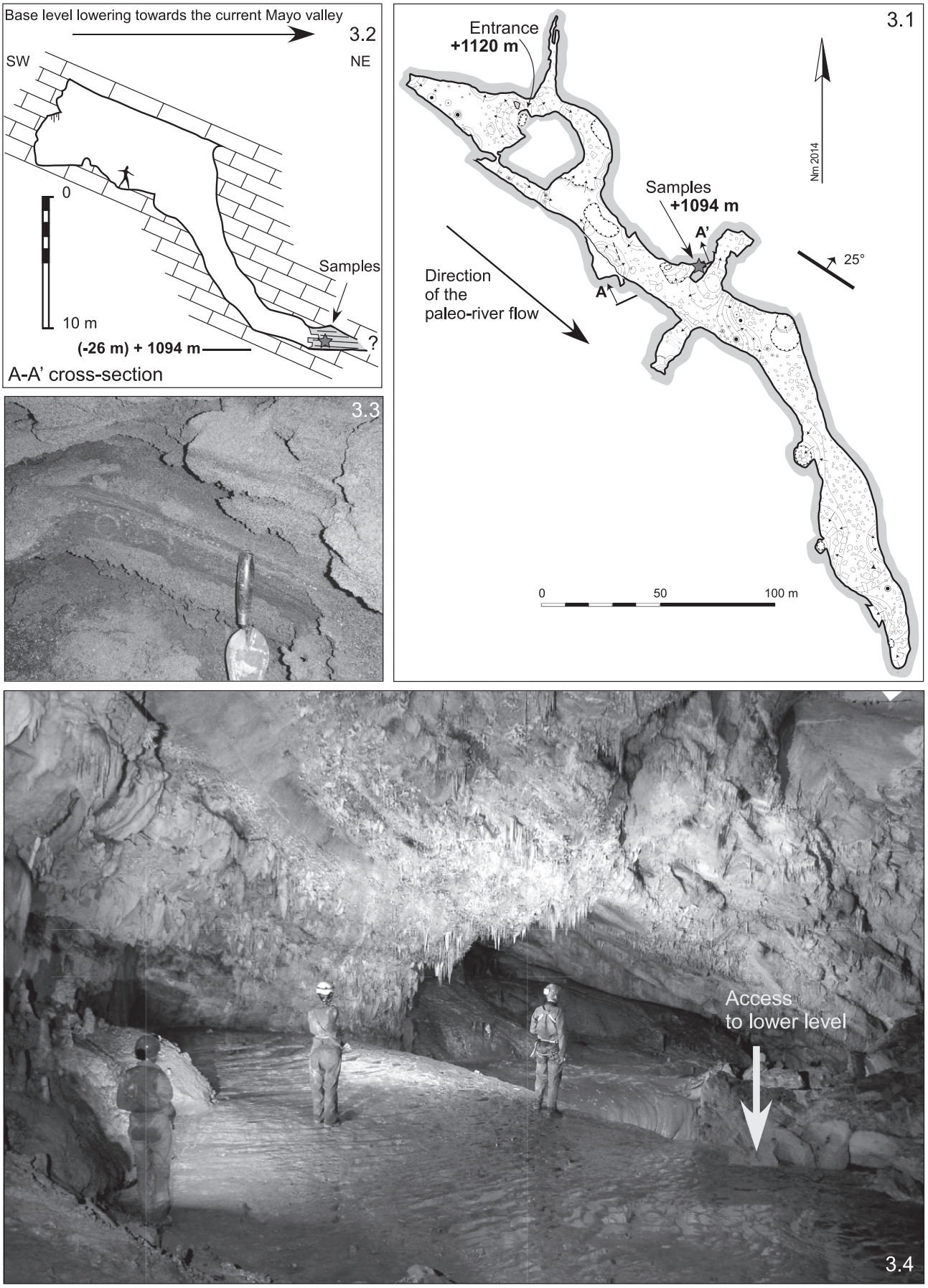

FIGURE 3 1- Topography of the Tishuca Cave (modified from Klein et al., 2015) with location of the sand samples and the cross-section A-A' displayed in Figure 3.2. 2- Cross-section through the Tishuca gallery with location of the sand samples. 3- Photograph of the sand outcrop. 4- Photograph of the upper level of the Tishuca gallery. [Colour figure can be viewed at wileyonlinelibrary.com]

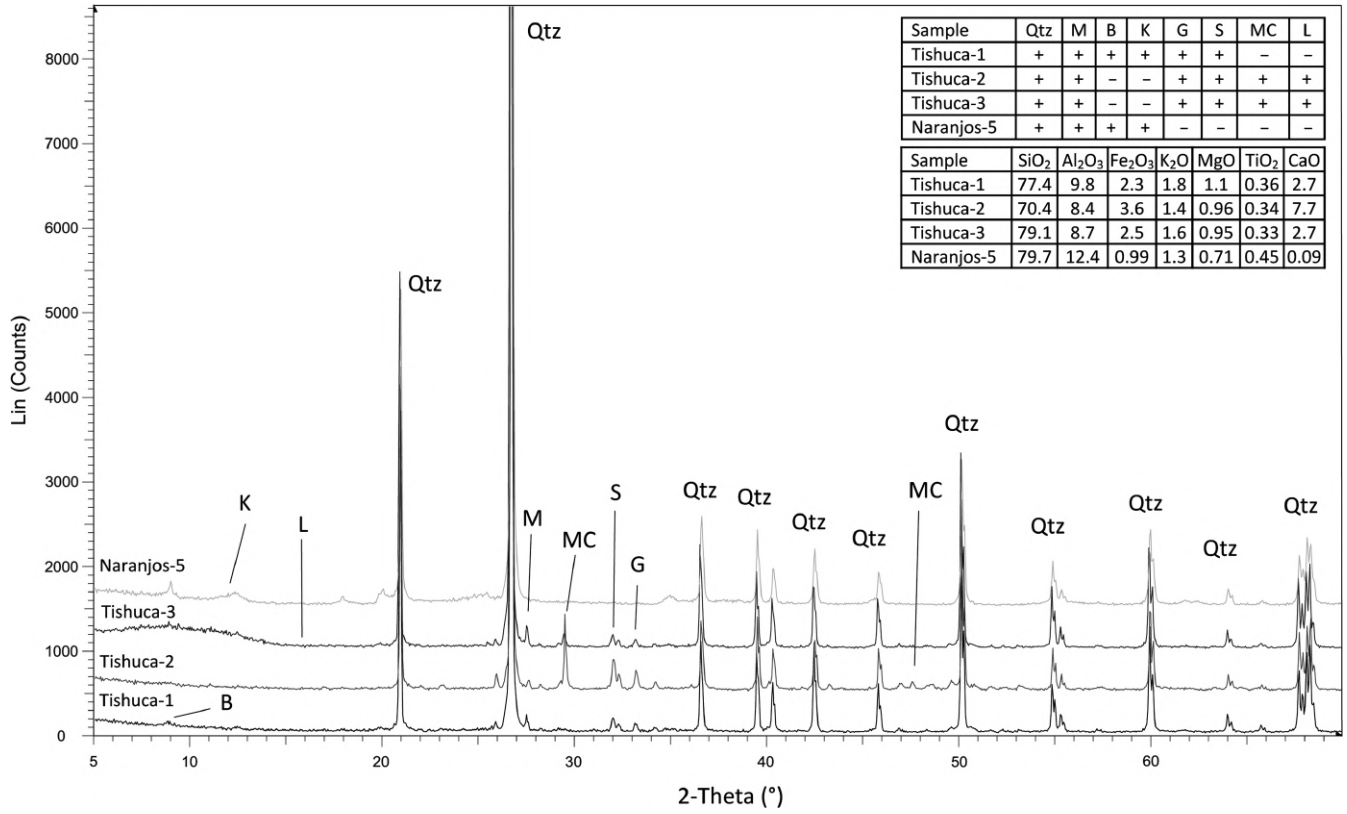

Sample	Qtz	M	B	K	G	S	MC	L
Tishuca-1	+	+	+	+	+	+	–	–
Tishuca-2	+	+	–	–	+	+	+	+
Tishuca-3	+	+	–	–	+	+	+	+
Naranjos-5	+	+	+	+	–	–	–	–

Sample	SiO_2	Al_2O_3	Fe_2O_3	K_2O	MgO	TiO_2	CaO
Tishuca-1	77.4	9.8	2.3	1.8	1.1	0.36	2.7
Tishuca-2	70.4	8.4	3.6	1.4	0.96	0.34	7.7
Tishuca-3	79.1	8.7	2.5	1.6	0.95	0.33	2.7
Naranjos-5	79.7	12.4	0.99	1.3	0.71	0.45	0.09

FIGURE 4 XRD whole-rock plots of the dated samples (Tishuca-1 to −3) and one sample from the Mayo River basin (Naranjos-5, see location in Figure 1). Mineral contents as well as major and selected minor elements obtained by XRF are shown in the top right tables. XRD and XRF data show a consistent mineralogical and geochemical composition between the samples. Mineral abbreviations: Qtz, quartz; M, microcline; Bt, biotite, Kln, kaolinite; Gt, goethite; Sd, siderite; MC, magnesium calcite. [Colour figure can be viewed at wileyonlinelibrary.com]

bleaching. The CAM provided D_es that resulted in consistent ages. Due to the low D_rs, typical for sediments in limestone caves and the dim OSL signals, the dispersion observed in the samples was attributed to beta microdosimetry (Mayya et al., 2006) and the dim signals (Ballarini et al., 2003).

The three studied samples correspond to the same deposit that was formed during a short-lived depositional event. The three obtained ages are equal with respect to their 1σ standard deviation interval (Table 1), making it possible to calculate a common age of 70.4 ± 6.2 ka (1σ standard deviation) based on the weighted mean of the three ages, assuming a single depositional event. By dividing the altitude difference (159 m) between the samples location in the cave and the present-day river channel (local base level) by the OSL age obtained in the Tishuca Cave sands, an average incision rate since 70.4 ka for the Mayo River was calculated at 2.3 mm a^{-1}. This value can be considered as a minimum if the sands are reworked and come from the upper level of the cave. In that case the incision rate would be 2.6 mm a^{-1}.

5 | DISCUSSION

The observed dim OSL signals are usually found in quartz grains of sediments that have an Andean source, as reflected in some previous studies. In a study of sediments of the Pisco Valley in the Peruvian forearc, Steffen et al. (2009) observed that, apart from the dim signals of quartz grains, the OSL decay curves were slow. They studied the OSL signals and identified a thermally unstable intermediate OSL component that caused an underestimation of the true age of the sediments. Other studies of Quaternary sediments of the Peruvian forearc (Trauerstein et al., 2014) and of the Atacama Desert in Chile (Rio et al., 2019) indicated a similar behaviour. However, a recent study of fluvial sediments in the intermontane Huancayo basin, located in the central Peruvian Andes, provided reliable quartz OSL ages that matched radiocarbon ages of the same sediments (Viveen et al., 2019). In that study slow and unstable OSL signals or components were not observed. Another recent study of Quaternary fluvial sediments from the Huallaga basin, located some hundred kilometres south of Cerro Blanco, showed unstable OSL components in only two out of eight quartz samples (Viveen et al., 2020). This suggests that a possible origin of the unstable OSL components may be the Andean source of quartz grains, and the potential use of quartz for OSL dating probably depends on the geology of the studied basin. The quartz sand grains of the Tishuca Cave deposits were sourced from upstream by Cretaceous fluvio-deltaic quartz-rich sandstones and Jurassic fluvial reddish sandstones inter-bedded with siltstones. The quartz sand grains from the Quaternary sediments of the Huallaga Basin (Viveen et al., 2020) originate from the

TABLE 1 Results of OSL dating: depth of the samples in the sediment, activity concentrations of radioisotopes, estimated beta (D_β), gamma + cosmic ($D_\gamma + D_c$) and total (D_r) dose-rate, number of accepted/measured aliquots (N), De, Overdispersion of the mean (Ov.) Dose recovery ratio (DRC), DRC overdispersion (DRC Ov.) and resulting ages for the studied samples

Sample	Depth (m)	^{238}U (Bq/kg)	^{232}Th (Bq/kg)	^{40}K (Bq/kg)	D_β (Gy/ka)	$D_\gamma + D_c$ (Gy/ka)	D_r (Gy/ka)	N	D_e (Gy)	Ov. (%)	Dose Recovery ratio	DRC Ov. (%)	Age (ka)
Tishuca-1	0.2	32.3 ± 1.5	11.5 ± 1.3	122 ± 10	0.50 ± 0.03	0.46 ± 0.02	0.97 ± 0.04	42/212	67.12 ± 5.37	46.3 ± 6.2	0.91 ± 0.01	20 ± 13	69.5 ± 6.1
Tishuca-2	1.6	38.4 ± 2.0	9.9 ± 0.7	108 ± 25	0.52 ± 0.05	0.43 ± 0.08	0.96 ± 0.10	49/226	61.65 ± 4.08	39.1 ± 5.4	0.91 ± 0.03	13 ± 9	64.4 ± 7.7
Tishuca-3	0.8	40.6 ± 2.2	11.8 ± 0.7	115 ± 11	0.58 ± 0.03	0.52 ± 0.02	1.08 ± 0.04	47/197	83.24 ± 4.36	31.1 ± 4.2	0.92 ± 0.01	12 ± 6	77.3 ± 4.9

same rocks, and probably from metamorphic rocks located farther away, that could explain the two samples with unstable OSL components. Our results are therefore consistent with the results from these studies.

The Mayo River floodplain of the Moyobamba Basin corresponds to the drained, clastic piedmont of the Cerro Blanco mountain belt. In such a morphotectonic setting, where the clastic piedmont is in direct contact with the active fold-and-thrust belt and disconnected from a marine base level, it is usually accepted that river incision deduced from cave level development is directly related to tectonic uplift in real time (Audra & Palmer, 2013; Calvet et al., 2015; Harmand et al., 2017). In such case, river incision had to keep pace with tectonic uplift (Bull, 1991), and given sufficient time has passed, a graded concave-shaped river profile will have developed (Hack, 1973). The profile of the Mayo River is indeed concave (Figure 7), suggesting near-equilibrium conditions. River profiles in equilibrium conditions are typically modelled by power or logarithmic functions (Snow & Slingerland, 1987). In both cases, the Mayo River profile can be successfully modelled with a best-fit R^2 of 0.97 and 0.95, respectively. Applying e.g. the power function, a modelled elevation value of 938 m. asl. is obtained for the Mayo floodplain below the Tishuca cave entrance, whereas a value of 934 m asl. was measured on the SRTM3 DEM, and a value of 935 m was obtained from topographic measurements in the field. The SRTM3 DEM has a vertical root mean square error of only 5.5 m in the Moyobamba basin (Gonzalez-Moradas & Viveen, 2020) and the modelled/measured elevation values are therefore consistent. Thus, we consider that the Mayo River incision, deduced from the Tishuca Cave sands dating, can be used as a reliable proxy for tectonic uplift.

A tectonic uplift rate of 2.3 to 2.6 mm a^{-1} calculated for the last 70 ka, which is consistent with the orogenic context of the region (Calderon, Baby, Hurtado, et al., 2017). This value is comparable with the Biabo anticline uplift rate of 2.0 mm a^{-1} for the past 46 ka in the neighbouring Huallaga basin, as recently calculated from folded fluvial terraces (Viveen et al., 2020). In the Huallaga Basin, long-term thrust-related uplift can also be calculated for structures comparable to the Cerro Blanco anticline using thermochronologic data. One surface sample from the youngest west-verging basement thrust structure of the Huallaga Basin (Cushabatay High) gave an AFT age of 5.8 Ma (Calderon, Baby, Vela, et al., 2017). Using a regional geothermal gradient of 20.1°C/km (Eude et al., 2015), an average tectonic uplift rate of ~ 0.75 mm a^{-1} can be calculated for the past 5.8 Ma. This uplift rate is three times less than that of Cerro Blanco, and shows that it is difficult to compare long-term with short-term deformation. Indeed, the long-term propagation of a thrust fault in fold-and-thrust belts is not continuous and depends on the critical taper of the wedge (Dahlen, 1990).

The Cerro Blanco uplift rate is coherent with the strong tectonic activity that characterises the Moyobamba region (Calderon, Baby, Hurtado, et al., 2017; Tavera et al., 2001) and directly linked to the active propagation of west-verging basement thrusts (Figure 2). During the last 70 ka, the uplift of the eastern limb of the Cerro Blanco anticline has also provoked a shift of the Mayo River by some

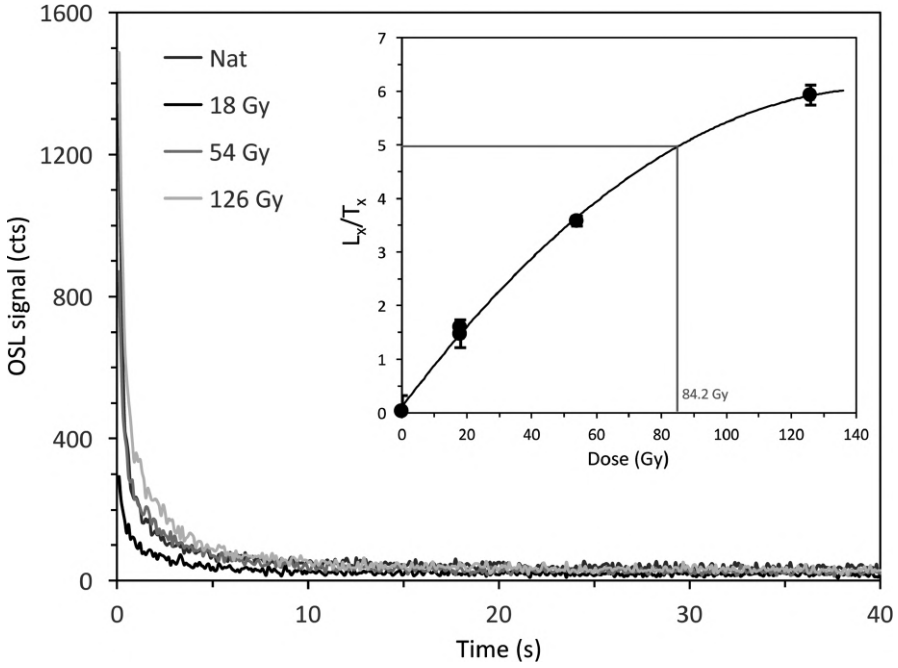

FIGURE 5 Example of typical natural and regenerated OSL decay curves observed in the studied samples. The example corresponds to an aliquot of sample Tishuca-3. In the inset the dose-response curve of the same aliquot is shown. The red horizontal line of the inset shows the Lx/Tx value of the aliquot and the red vertical line the corresponding D_e (84.2 Gy). L_x/T_x is the ratio between the initial OSL signal minus background, estimated from the last part of the stimulation curve measured from the natural or a regenerated dose (L_x) and the OSL signal measured after administrating a test dose (T_x) (Murray & Wintle, 2000). [Colour figure can be viewed at wileyonlinelibrary.com]

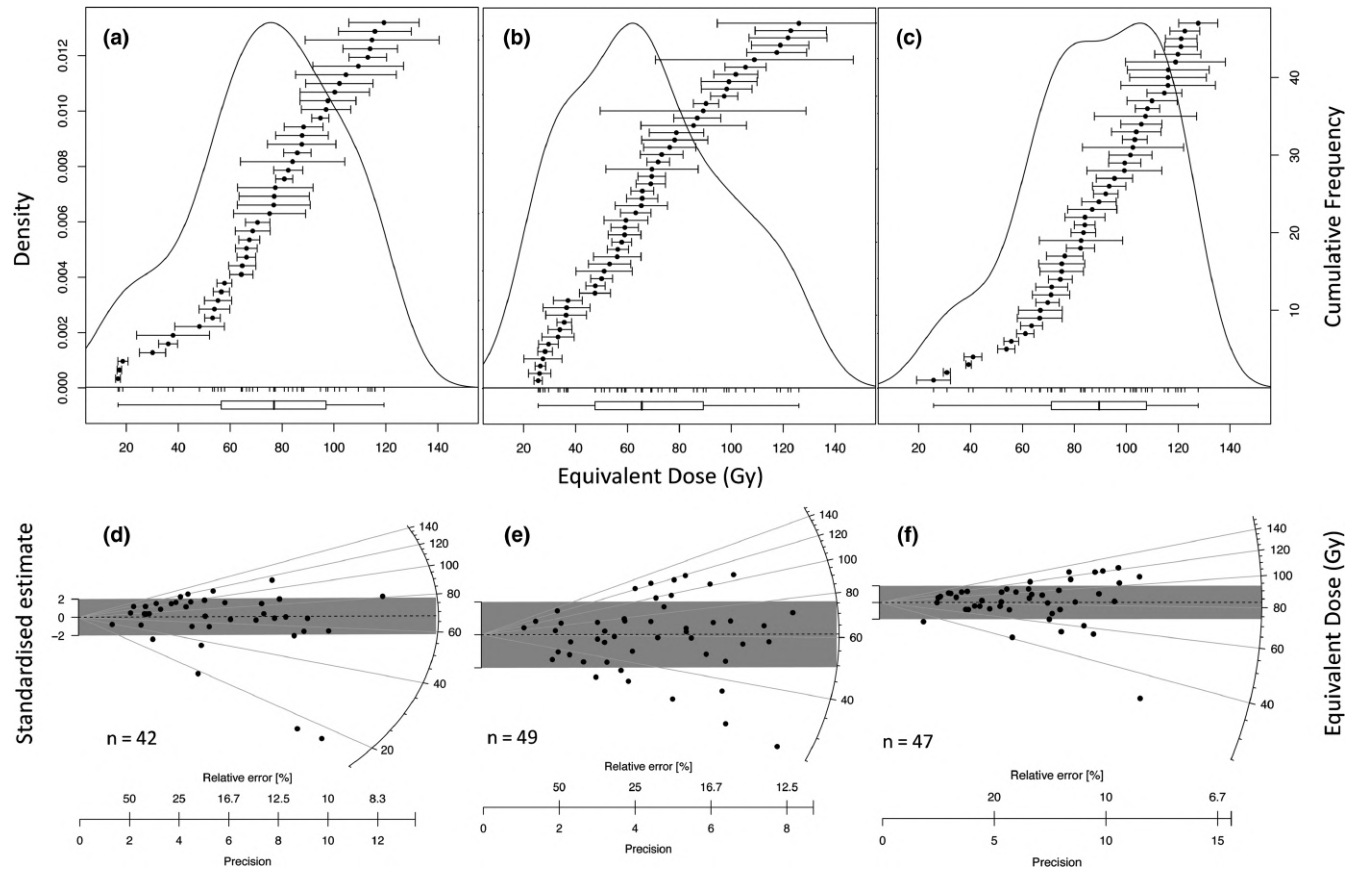

FIGURE 6 Kernel Density Estimation plots (A, B, C) and Radial Plots (D, E, F) of the studied samples with the distribution of D_es of multigrain aliquots. (A, D) Tishuca-1, (B, E) Tishuca-2, (C, F) Tishuca-3. The errors of aliquots provided in figures A, B and C correspond to 1-sigma intervals. Radial plots were drawn using the application of Burow (2016). The grey bar in radial plots corresponds to the central D_es estimated for each sample. Non-skewed distributions are observed in all samples with high dispersion of aliquots.

1,000 m to the NE. The Cerro Blanco uplift rate is similar to the late Quaternary uplift rates of the Subandes in Colombia (2.8 mm a^{-1}; Veloza et al., 2015) and Venezuela (1.1 mm a^{-1}; Guzman et al., 2013). But it is lower than Quaternary uplift rates of others mountain belts, such as e.g. the 10 mm a^{-1} of the Main Frontal Thrust of the Himalaya (Lavé & Avouac, 2001).

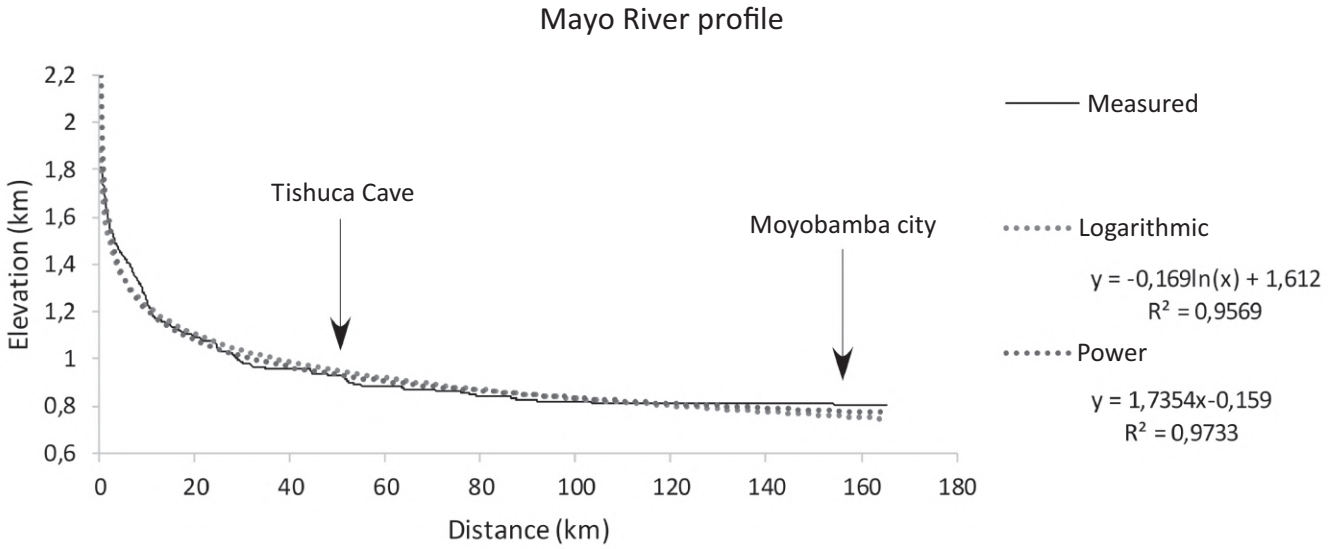

FIGURE 7 Mayo River profile from its source to the outlet of the Moyobamba basin just south of Moyobamba city, based on the Shuttle Radar Topography Mission version 3 (SRTM3) DEM. The concave-up shape profile suggests that river incision keeps pace with tectonic uplift. Trend lines of the profile data based on power and logarithmic functions show very high R^2 correlations, reinforcing that the Mayo River is in dynamic equilibrium conditions. [Colour figure can be viewed at wileyonlinelibrary.com]

6 | CONCLUSIONS

The discovery of a horizontal cave containing datable fluvial deposits in the NE Peru has allowed to calculate a tectonic uplift rate of 2.3 to 2.6 mm a^{-1} for the last 70 ka. This tectonic uplift rate is the first one calculated from fluvial cave sands in the Andes and the Tropical Zone, and one of the very few late Quaternary uplift rates available so far for the entire South American Subandes. The results confirm that dating of fluvial sands in caves is a powerful tool to quantify Quaternary incision and uplift rates of active mountain fronts.

In all the caves we explored in the Cerro Blanco karst, we found damaged speleothems attesting to the strong seismic activity linked to the anticline. A detailed study of these speleothems could further help to constrain the chronology of the seismic events related to the high tectonic activity in the area.

ACKNOWLEDGEMENTS

We express our gratitude to Groupe Spéléologique Bagnols Marcoule and Espeleo Club Andino that mapped the Tishuca Cave. Research funding of the Pontificia Universidad Católica del Perú to W. Viveen (project grant 461) made the fieldwork for OSL sampling and dating of the cave sands possible. JC. Villegas received support from the IPGH PAT-GEOF07. Petroleum Experts are acknowledged for providing an academic license of the "MOVE" software. The University Institute of Geology of the University of A Coruña (Spain) received support from the Xunta de Galicia, Spain (GPC2015/024 and R2017/008). Editor Klaus Mezger, reviewer Marc Calvet and an anonymous reviewer are kindly acknowledged for their constructive comments.

CONFLICT OF INTEREST

None.

DATA AVAILABILITY STATEMENT

Data available on request from the authors.

REFERENCES

Antón, L., Rodés, A., De Vicente, G., Pallàs, R., Garcia-Castellanos, D., Stuart, F. M., Braucher, R., & Bourlès, D. (2012). Quantification of fluvial incision in the Duero Basin (NW Iberia) from longitudinal profile analysis and terrestrial cosmogenic nuclide concentrations. *Geomorphology*, *165–166*, 50–61.

Armijos, E., Crave, A., Vauchel, P., Fraizy, P., Santini, W., Moquet, J. S., Arevalo, N., Carranza, J., & Guyot, J. L. (2013). Suspended sediment dynamics in the Amazon River of Peru. *Journal of South American Earth Sciences*, *44*(SI), 75–84.

Audra, P., & Palmer, A. N. (2013). The vertical dimension of karst: controls of vertical cave pattern. In: J. F. Shroder Editor-in-chie & A. Frumkin Volume Editor. *Treatise on Geomorphology*, (*6*, 186–206). Karst Geomorphology. : Academic Press.

Ballarini, M., Wallinga, J., Murray, A. S., van Heteren, S., Oost, A. P., Bos, A. J. J., & van Eijk, C. W. E. (2003). Optical dating of young coastal dunes on a decadal time scale. *Quaternary Science Reviews*, *22*, 1011–1017.

Bès de Berc, S. B., Soula, J. C., Baby, P., Souris, M., Christophoul, F., & Rosero, J. (2005). Geomorphic evidence of active deformation and uplift in a modern continental wedge-top - Foredeep transition: Example of the eastern Ecuadorian Andes. *Tectonophysics*, *399*, 351–380. https://doi.org/10.1016/j.tecto.2004.12.030

Bigot, J. Y., Guyot, J. L., Robert, X., & Apaéstegui, J. (2018). Pérou, Expédition spéléo-scientifique "Cerro Blanco 2017". *Spelunca*, *150*, 5–9.

Brennan, B. J. (2003). Beta doses to spherical grains. *Radiation Measurements*, *3*, 299–303.

Bridgland, D., & Westaway, R. (2008). Climatically controlled river terrace staircases: A worldwide Quaternary phenomenon. *Geomorphology*, *98*, 285–315.

Bull, W. B. (1991). *Geomorphic Responses to Climatic Change*. Oxford University Press.

Burbank, D. W., & Anderson, R. S. (2011). *Tectonic Geomorphology* (2nd edn). John Wiley & Sons. https://doi.org/10.1002/9781444345063

Burow, C. (2016). RLumShiny: 'Shiny' Applications for the R Package 'Luminescence'. https://CRAN.R-project.org/package=RLumShiny. R package version 0.1.1

Calderon, Y., Baby, P., Hurtado, C., & Brusset, S. (2017). Thrust tectonics in the Andean retro-foreland basin of northern Peru: Permian inheritances and petroleum implications. *Marine and Petroleum Geology*, *82*, 238–250. https://doi.org/10.1016/j.marpetgeo.2017.02.009

Calderon, Y., Baby, P., Vela, C., Hurtado, A., Eude, A., Roddaz, M., Brusset, S., Calvés, G., & Bolaños, R. (2017). Petroleum systems restoration of the Huallaga-Marañon Andean retroforeland basin, Peru. *Petroleum Systems Analysis-Case Studies*, *AAPG Memoir*, *114*, 95–116. https://doi.org/10.1306/13602026M1143702

Calvet, M., Gunnell, Y., Braucher, R., Hez, G., Bourlès, D., Guillou, V., & Delmas, M. (2015). Cave levels as proxies for measuring post- orogenic uplift: Evidence from cosmogenic dating of alluvium-filled caves in the French Pyrenees. *Geomorphology*, *246*, 617–633. https://doi.org/10.1016/j.geomorph.2015.07.013

Dahlen, F. A. (1990). Critical taper model of fold-and-thrust belts and accretionary wedges. *Annual Review of Earth & Planetary Sciences*, *18*, 55–99. https://doi.org/10.1146/annurev.ea.18.050190.000415

de Río, I., Sawakuchic, A. O., & González, G. (2019). Luminescence dating of sediments from central Atacama Desert, northern Chile. *Quaternary Geochronology*, *53*, 101002. https://doi.org/10.1016/j.quageo.2019.05.001

Devlin, S., Isacks, B. L., Pritchard, M. E., Barnhart, W. D., & Lohman, R. B. (2012). Depths and focal mechanisms of crustal earthquakes in the central Andes determined from teleseismic waveform analysis and InSAR. *Tectonics*, *31*, 1–33. https://doi.org/10.1029/2011TC002914

Eude, A., Roddaz, M., Brichau, S., Brusset, S., Calderon, Y., Baby, P., & Soula, J. C. (2015). Controls on timing of exhumation and deformation in the northern Peruvian eastern Andean wedge as inferred from low-temperature thermochronology and balanced cross section. *Tectonics*, *34*, 715–730. https://doi.org/10.1002/2014TC003641

Galbraith, R. F., Roberts, R. G., Laslett, G. M., Yoshida, H., & Olley, J. M. (1999). Optical dating of single and multiple grains of quartz from Jinmi-um Rock Shelter, northern Australia: Part I, experimental design and statistical models. *Archaeometry*, *41*, 339–364. https://doi.org/10.1111/j.1475-4754.1999.tb00987.x

González-Moradas, M. R., & Viveen, W. (2020). Evaluation of ASTER GDEM2, SRTMv3.0, ALOS AW3D30 and TanDEM-X DEMs for the Peruvian Andes against highly accurate GNSS ground control points and geomorphological-hydrological metrics. *Remote Sensing of Environment*, *237*, 111509. https://doi.org/10.1016/j.rse.2019.111509

Guérin, G., Mercier, N., & Adamiec, G. (2011). Dose-rate conversion factors: Update. *Ancient TL*, *29*, 5–8.

Guzmán, O., Vassallo, R., Audemard, F., Mugnier, J. L., Oropeza, J., Yepez, S., Carcaillet, J., Alvarado, M., & Carrillo, E. (2013). 10Be dating of river terraces of Santo Domingo river, on Southeastern flank of the Mérida Andes, Venezuela: Tectonic and climatic implications. *Journal of South American Earth Sciences*, *48*, 85–96. https://doi.org/10.1016/j.jsames.2013.09.004

Hack, J. T. (1973). Stream-profile analysis and stream-gradient index. U.S. *Geological Survey Journal of Research*, *1*, 421–429.

Haeuselmann, P., Granger, D. E., Jeannin, P. Y., & Lauritzen, S. E. (2007). Abrupt glacial valley incision at 0.8 Ma dated from cave deposits in Switzerland. *Geology*, *35*, 143–146. https://doi.org/10.1130/G23094A

Harmand, D., Adamson, K., Rixhon, G., Jaillet, S., Losson, B., Devos, A., Hez, G., Calvet, M., & Audra, P. (2017). Relationships between fluvial evolution and karstification related to climatic, tectonic and eustatic forcing in temperate regions. *Quaternary Science Reviews*, *166*, 1–19. https://doi.org/10.1016/j.quascirev.2017.02.016

Klein, J. D., Bigot, J. Y., & Guyot, J. L. (2015). Pérou, Nueva Cajamarca 2014. *Spelunca*, *139*, 5–9.

Klein, J. D., Bigot, J. Y., & Guyot, J. L. (2016). Pérou, Expédition spéléo-scientifique "Cerro Blanco 2017". *Spelunca*, *150*, 5–9.

Lavé, J., & Avouac, J. P. (2001). Fluvial incision and tectonic uplift across the Himalayas of central Nepal: Journal of Geophysical Research. *Solid Earth*, *106*, 26561–26591. https://doi.org/10.1029/2001jb000359

Liu, Y. U., Wang, S., Xu, S., Liu, X., Fabel, D., Zhang, X., Luo, W., & Cheng, A. (2014). New evidence for the incision history of the Liuchong River, Southwest China, from cosmogenic 26 Al / 10 Be burial ages in cave sediments. *Journal of Asian Earth Sciences*, *73*, 274–283. https://doi.org/10.1016/j.jseaes.2013.04.044

Mayya, Y. S., Morthekai, P., Murari, M. K., & Singhvi, A. K. (2006). Towards quantifying beta microdosimetric effects in single-grain quartz dose distribution. *Radiation Measurements*, *41*, 1032–1039. https://doi.org/10.1016/j.radmeas.2006.08.004

Miall, A. D. (1996). *The geology of fluvial deposits: Sedimentary facies*, *basin analysis and petroleum geology* (p. 582). Springer.

Murray, A. S., & Wintle, A. G. (2000). Luminescence dating of quartz using an improved single-aliquot regenerative-dose protocol. *Radiation Measurements*, *32*, 57–73. https://doi.org/10.1016/S1350-4487(99)00253-X

Murray, A. S., & Wintle, A. G. (2003). The single aliquot regenerative dose protocol: Potential for improvements in reliability. *Radiation Measurements*, *37*, 377–381. https://doi.org/10.1016/S1350-4487(03)00053-2

Prescott, J. R., & Hutton, J. T. (1994). Cosmic ray contributions to dose rates for luminescence and ESR dating: Large depths and long term variations. *Radiation Measurements*, *23*, 497–500.

Robert, X., Bigot, J.-Y., Guyot, J.-L., Lips, B., Lips, J., Pouilly, M., Picque, C., Klein, J.-D., Baby, P., & De Pomar, A. (2020). Nor Peru 2019. *Bulletin ECA-GSBM-GSD-GSVulcain*. https://www.gsbm.fr/publications/gsbm/2020_NordPerou-2019/NordPerou2019.pdf

Rodríguez, R., Cueva, E., Sánchez, E., Ojeda, D., Fabian, C., & Giraldo, E. (2017). Geología del cuadrángulo de Rioja, hoja 13i. *INGEMMET*, *Boletín*, *Serie A: Carta Geológica Nacional (Escala 1:50 000)*, *150*, 82, 4 mapas.

Rosas, S., Fontboté, L., & Tankard, A. (2007). Tectonic evolution and paleogeography of the Mesozoic Pucará Basin, central Peru. *Journal of South American Earth Sciences*, *24*, 1–24. https://doi.org/10.1016/j.jsames.2007.03.002

Snow, R. S., & Slingerland, R. L. (1987). Mathematical Modeling of Graded River Profiles. *The Journal of Geology*, *95*(1), 15–33. https://doi.org/10.1086/629104

Steffen, D., Preusser, F., & Schlunegger, F. (2009). OSL quartz age underestimation due to unstable signal components. *Quaternary Geochronology*, *4*(5), 353–362. https://doi.org/10.1016/j.quageo.2009.05.015

Stock, G. M., Anderson, R. S., & Finkel, R. C. (2005). Rates of erosion and topographic evolution of the Sierra Nevada, California, inferred from cosmogenic 26Al and 10Be concentrations. *Earth Surface Processes and Landforms*, *30*, 985–1006. https://doi.org/10.1002/esp.1258

Stock, G. M., Granger, D. E., Sasowsky, I. D., Anderson, R. S., & Finkel, R. C. (2005). Comparison of U-Th, paleomagnetism, and cosmogenic burial methods for dating caves: Implications for landscape evolution studies. *Earth and Planetary Science Letters*, *236*, 388–403. https://doi.org/10.1016/j.epsl.2005.04.024

Tavera, H., Buforn, E., Bernal, I., & Antayhua, Y. (2001). Analysis of the rupture processes of 1990 and 1991 alto mayo valley earthquakes (Moyobamba, Perú). *Boletín De La Sociedad Geológica Del Perú*, *91*, 55–68. (in Spanish).

Trauerstein, M., Lowick, S. E., Preusser, F., & Schlunegger, F. (2014). Small aliquot and single grain IRSL and post-IR IRSL dating of fluvial and alluvial sediments from the Pativilca valley, Peru. *Quaternary Geochronology*, *22*, 163–174. https://doi.org/10.1016/j.quageo.2009.05.015

Veloza, G., Taylor, M., Mora, A., & Gose, J. (2015). Active mountain building along the eastern Colombian Subandes: A folding history from deformed terraces across the Tame anticline, Llanos Basin. *Geological Society of America Bulletin*, *127*, 1155–1173. https://doi.org/10.1130/B31168.1

Villegas-Lanza, J. C., Chlieh, M., Cavalié, O., Tavera, H., Baby, P., Chire-Chira, J., & Nocquet, J. M. (2016). Active tectonics of Peru: Heterogeneous interseismic coupling along the Nazca megathrust, rigid motion of the Peruvian Sliver, and Subandean shortening accommodation. *Journal of Geophysical Research: Solid Earth*, *121*, 7371–7394. https://doi.org/10.1002/2016JB013080

Viveen, W., Baby, P., Sanjurjo-Sanchez, J., & Hurtado-Enriquez, C. (2020). Fluvial terraces as quantitative markers of late Quaternary detachment folding and creeping thrust faulting in the Peruvian Huallaga River basin. *Geomorphology*, *367*, 107315. https://doi.org/10.1016/j.geomorph.2020.107315

Viveen, W., Sanjurjo-Sánchez, J., Goy-Diz, A., Veldkamp, A., & Schoorl, J. M. (2014). Paleofloods and ancient fishing weirs in NW Iberian rivers. *Quaternary Research*, *82*, 56–65. https://doi.org/10.1016/j.yqres.2014.04.011

Viveen, W., Schoorl, J. M., Veldkampc, A., van Balend, R. T., Desprate, S., & Vidal-Romanibet, J. R. (2013). Reconstructing the interacting effects of base level, climate, and tectonic uplift in the lower Miño terrace record: A gradient modelling evaluation. *Geomorphology*, *186*, 96–118.

Viveen, W., Zevallos-Valdivia, L., & Sanjurjo-Sanchez, J. (2019). The influence of centennial-scale variations in the South American summer monsoon and base-level fall on Holocene fluvial systems in the Peruvian Andes. *Global and Planetary Change*, *176*, 1–22. https://doi.org/10.1016/j.gloplacha.2019.03.001

Wagner, T., Fritz, H., Stüwe, K., Nestroy, O., Rodnight, H., Hellstrom, J., & Benischke, R. (2011). Correlations of cave levels, stream terraces and planation surfaces along the River Mur-Timing of landscape evolution along the eastern margin of the Alps. *Geomorphology*, *134*, 62–78. https://doi.org/10.1016/j.geomorph.2011.04.024

How to cite this article: Baby P, Viveen W, Sanjurjo-Sanchez J, et al. First record of OSL-dated fluvial sands in a tropical Andean cave reveals rapid late Quaternary tectonic uplift. *Terra Nova*. 2021;33:262–273. https://doi.org/10.1111/ter.12512